

Adsorption and photocatalytic degradation investigation of organic dyes on TiO₂ bentonite surface in aqueous solution

Rachid Cherouaki^{a,b,*}, Youssef Gherraby^a, Rajaa Bassam^a, Said Belaaouad^a, Jamal Naja^b

^aLaboratory of Physical Chemistry of Materials LCPM, Faculty of Sciences Ben M'Sik, Hassan II University of Casablanca, B.P.7955, Bd Cdt_Driss El Harti, Morocco, Tel.: +212671678715; email: rachid.cherouaki@gmail.com (R. Cherouaki), Tel.: +212663291616; email: youssef.gherraby-etu@etu.univh2c.ma (Y. Gherraby), Tel.: +212688400451; email: bassam.rajaa@gmail.com (R. Bassam), Tel.: +212633160204; email: sbelaouad@yahoo.fr (S. Belaaouad)

^bApplied Chemistry and Environment Laboratory, University of Science and Technology Settat 577, Morocco, Tel.: +212661472237; email: jamal.naja@uhp.ac.ma

Received 28 August 2022; Accepted 14 March 2023

ABSTRACT

This work investigates the adsorption and the photocatalytic degradation performance of dyes (methylene blue (MB) and methyl orange (MO)) on the surface of raw bentonite (Raw-B) and doped bentonite with titanium oxide (TiO₂-B). The bentonite was selected from the Nador region in northern Morocco, it was doped with various TiO₂ mass ratios. The structural, mineralogical and morphological composition of Raw-B and TiO₂-B was characterized using several techniques including inductively coupled plasma atomic emission spectroscopy, X-ray diffraction, Fourier-transform infrared, transmission electron microscopy, and energy-dispersive X-ray analysis. The adsorption process of MB and MO were affected according to the Langmuir and Freundlich isotherms. The maximum removal capacity of MB and MO were around 60.97 and 142.85 mg/g, respectively. MB and MO degradation ratios achieved 100% under a lamp irradiation at 245 nm. The results obtained show that the application of titanium oxide-doped bentonite has a very high performance in wastewater treatment.

Keywords: Adsorption; Photocatalytic degradation; TiO₂-Bentonite; Methylene blue; Methyl orange

1. Introduction

In general, water pollution is produced from several sources, especially from agricultural, urban and industry, this contamination has a harmful effect on the quality of water resources. Organic pollutants are a great risk to human health and the environment since to their application in several sectors, their accumulation and their resistance to biodegradability [1,2]. The dyeing and textile industries are the most water consuming [3,4]. Methylene blue and methyl orange are among the dyes that have a toxic effect on living beings and on the environment [5–7], which

necessitates the improvement of effective means for the protection of water against pollution.

Numerous water treatment methods were applied to reduce the contamination of aquatic environments by these pollutants including biology, photocatalytic degradation, membrane technique, adsorption and coagulation–flocculation [8–11]. Adsorption and photocatalytic degradation were the most used methods in the removal of textile dyes with high efficiency. The adsorption processes consist of fixing molecules on the surface of solids using specific interactions or covalent bonds. Biomasses, algae, soils, activated carbon, clay and agricultural solid waste were among the materials that show promising profitability as

* Corresponding author.

adsorbents of dye pollutants [12–16]. Therefore, photocatalytic degradation is a technique that allows the degradation of organic molecules using a photocatalyst and UV radiation. The semi-conductors such as ZrO_2 , V_2O_5 , TiO_2 and ZnO were widely used as photocatalysts for the degradation of organic pollutants [17–19].

Various works in the literature study the adsorption and the photodegradation of methylene blue and methyl orange using different adsorbents [20–25]. Oyarce et al. [26] has investigated the adsorption of methylene blue (MB) and methyl orange (MO) with water soluble polymers PAMPS (poly (2-acrylamide-2-methyl-1-propanesulfonic acid)) and PDDA (polydiallyldimethylammonium) in an aqueous medium. The maximum adsorption capacity of the dyes was around 90% for MO at an initial concentration of 80 mg/L, while the maximum removal efficiency of MB with the initial concentration of 3.5 mg/L was achieved at 98%. The adsorption process of MB and MO was realized in an acid medium of pH = 6 with a polymer/dye molar ratio of 10:1 for PDDA and 20:1 for PAMPS. It was observed that the Langmuir mode was the most suitable for the adsorption of MB and MO onto PAMPS and PDDA. The regeneration study shows that PAMPS was regenerated for four or more cycles, whereas PDDA was regenerated only for four cycles since of its low desorption efficiency of MB and MO. However, the synthesis of silver-associated ZnO nanocomposite (AZ) using the coprecipitation method was performed by Stanley in the photocatalyst degradation of MB, MO, and RhB under sunlight irradiation in an aqueous solution [27]. A high degradation efficiency of MB was detected at 98.5% using 100 mg of AZ for 30 min. While the degradation efficiency of RhB was around 98.51% in 60 min with 60 mg of AZ. The high degradation efficiency of MB, MO and RhB were probably due to particle forms including nanoballs, nanorods, and nanoplates.

TiO_2 was applied several times as base photocatalysts for dyes degradation owing to its low cost, UV optical absorption, and stability [28–30]. The natural clay materials are generally more used as adsorbents and photocatalysts due to their different physico-chemical properties such as high cationic exchange capacity and large specific surface area [31–33]. However, the development of new cost-effective, efficient and ecofriendly materials for the treatment of dyes molecules is still of great environmental and scientific interest. In this context, the present work interest on the adsorption and the photocatalyst degradation of MB and MO using raw and modified bentonite by TiO_2 in aqueous medium. The preparation and the characterization of modified bentonite were studied with different physico-chemical characterizations. The adsorption process of MB and MO onto modified bentonite was performed according to several factors including contact time, TiO_2 ratio and hydrochloric acid. The kinetic and isotherm studies were also investigated. Therefore, the photocatalyst degradation of MB and MO was explored by varying the irradiation light.

2. Materials and methods

2.1. Preparation and characterization of TiO_2 -B

The synthesis of titanium oxide (TiO_2) was achieved by total dissolution of titanium tetrachloride in ethanol,

followed by evaporation and calcination at 500°C. The bentonite used in this work was collected from the Nador region in northern Morocco. The modification of bentonite by TiO_2 (TiO_2 -B) was carried out by the addition of bentonite in a TiO_2 solution synthesized with different precursors, the mixture was stirred at 450 rpm for 30 min to ensure homogenization of the solution, after the mixture was dried at 105°C for 12 h, the obtained powder was calcined at 500°C in an oven, with a temperature increase of 100°C/h.

The physico-chemical characterization of these samples was realized using diverse analytical methods. The chemical elements were determined using inductively coupled plasma atomic emission spectroscopy (ICP-AES) by THERMO FLASH2 spectrometry. The crystalline structure was identified by X-ray diffraction (XRD) using a SIEMENS D 500 diffractometer, equipped with a copper anticathode using monochromatic $K\alpha$ radiation of wavelength $\lambda = 1.54 \text{ \AA}$ at a voltage of 45 kV and an intensity of 30 mA. The Fourier-transform infrared spectroscopy (FTIR) show the vibrations of chemical bonds using a standard spectrometer (VERTEX 70). The morphology and the compositions of TiO_2 -B were determined by transmission electron microscopy (MET) coupled with energy-dispersive X-ray spectroscopy (EDX) by JEOL JEM 2010 device. The specific surface area was measured using an automated volumetric nitrogen adsorption device of the Micromeritics ASAP 2000 type.

2.2. Adsorption and photocatalytic degradation experiment

The process of adsorption of MB and MO onto TiO_2 -B was studied using 500 mL of aqueous solution with an initial concentration of 120 mg/L for MB, 40 mg/L for MO with 1 g/L of TiO_2 -B mass ratio under magnetic agitation of 250 rpm. The samples collected were filtered, centrifuged and analyzed by UV-visible spectrophotometry (wavelength of MB $\lambda = 670 \text{ nm}$ and $\lambda = 465 \text{ nm}$ for MO).

Therefore, the photocatalytic degradation of MB and MO was achieved by adding 1 g/L of TiO_2 -B in 500 mL of MB solutions with an initial concentration around 120 and 40 mg/L of MO under magnetic stirring of 250 rpm. The mixtures were irradiated with solar radiation and UV lamps of 245 and 365 nm as a source of excitation. After the photodegradation of MB and MO, the mixtures were filtered, centrifuged and analyzed by UV-visible spectrophotometry with the wavelength of MB around 670 and 465 nm for MO.

3. Results and discussion

3.1. Characterization of TiO_2 -B

The mineralogical composition of raw bentonite (Raw-B) and TiO_2 -B were detected using ICP-AES analysis as illustrated in Table 1. It was observed that the Raw-B was dominated by SiO_2 , Al_2O_3 and Na_2O with the trace of same minerals. After the modification of bentonite by TiO_2 , the ratio of TiO_2 increased, with the decreasing of SiO_2 , Al_2O_3 and Na_2O indicating the exchange between Si, Al, Na and Ti. The loss on ignition (LOI) values of Raw-B and TiO_2 -B did not exceed 11%, this result reflects the low value of organic material relative to the mineral fraction.

Fig. 1 shows the XRD patterns of Raw-B and TiO_2 -B. The X-ray diffraction characterization of Raw-B detects

the presence of montmorillonite at 19.923, 27.608, 44, and 62.382 Å. However, the XRD patterns of the various TiO₂-B samples show that the intense peaks characteristic of the TiO₂ phase were gradually increasing and it was observed an increasing in peak intensity at 31.707° and 45.465° and the appearance of new peaks at 2θ = 28.396°, 37.953°, 45.465° and 49.772°. The bentonite becomes more and more amorphous and the entity of the anatase TiO₂ lines increases at 2θ = 25°, the presence of other crystalline phases of TiO₂

Table 1
Chemical composition of TiO₂-B with different TiO₂ contents

Component (%)	TiO ₂ -B (0%)	TiO ₂ -B (5%)	TiO ₂ -B (10%)	TiO ₂ -B (15%)	TiO ₂ -B (20%)
SiO ₂	50.96	49.44	48.8	49.6	45
Al ₂ O ₃	24.46	24.52	22.5	24.1	22.3
TiO ₂	<<	1.56	4.45	9.11	14.6
Na ₂ O	7.257	6.594	6.81	6.36	6.26
MgO	1.522	1.36	1.36	1.85	1.66
Fe ₂ O ₃	1.635	1.969	1.726	1.54	1.61
Cl	3.188	2.954	1.13	1.19	1.53
CaO	0.802	0.767	0.763	0.772	0.592
K ₂ O	0.749	0.669	0.599	0.474	0.357
BaO	<<	<<	0.0232	0.142	0.178
P ₂ O ₅	0.0587	0.0523	0.0461	0.118	0.149
SO ₃	0.0276	0.0247	0.0338	0.101	0.0671
MnO ₂	0.0332	0.042	0.042	0.0503	0.0555
ZrO ₂	0.05	0.023	0.0116	0.04	0.0388
SrO	0.0088	0.0077	0.00641	0.0265	0.026
ThO ₂	<<	<<	0.00328	0.00633	0.0165
Y ₂ O ₃	<<	<<	0.00121	0.00299	0.00313
Rb	0.0057	0.0045	0.00535	0.00204	0.00244
Nb ₂ O ₅	<<	<<	0.0017	<<	0.00195
I	0.013	0.0128	0.0116	<<	<<
LOI	9.23	10	11.612	4.56	5.48

was more intense and the lines become very wide, with a very massive background noise, which could be due to the overlapping of the chemical elements of the different crystalline phases, or the first known evolution of the doping operation was the intercalation of TiO₂ at the bottom of the structure during the ionic exchange between sodium and titanium or the appearance of other mechanisms of chemical reaction that modify the nature of the structure.

The study of Raw-B and TiO₂-B by FTIR was used to detect the several chemical functions present on the surface of these matrix. Fig. 2 presents the FTIR spectra of Raw-B and TiO₂-B. The FTIR spectrum of Raw-B shows an intense absorption band between 450–550 cm⁻¹, which is probably attributed to the bending vibrations of Si–O–M band (M = Al, Fe, Mg...). The bands between 517 and 446 cm⁻¹ were mainly due to the bending vibrations of Si–O–Al and Si–O–Mg banding. The 800 cm⁻¹ band of Al–OH banding was shifted to low frequencies around 815 and 915 cm⁻¹. The hexagonal and rhombohedral carbonates were detected in 1,400 cm⁻¹ band [34], Therefore, the band that extends between 1,020

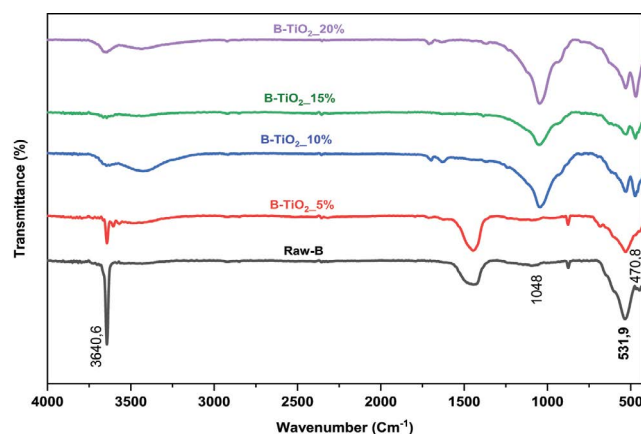


Fig. 2. Fourier-transform infrared spectra of Raw-B and TiO₂-B at different percentages of TiO₂.

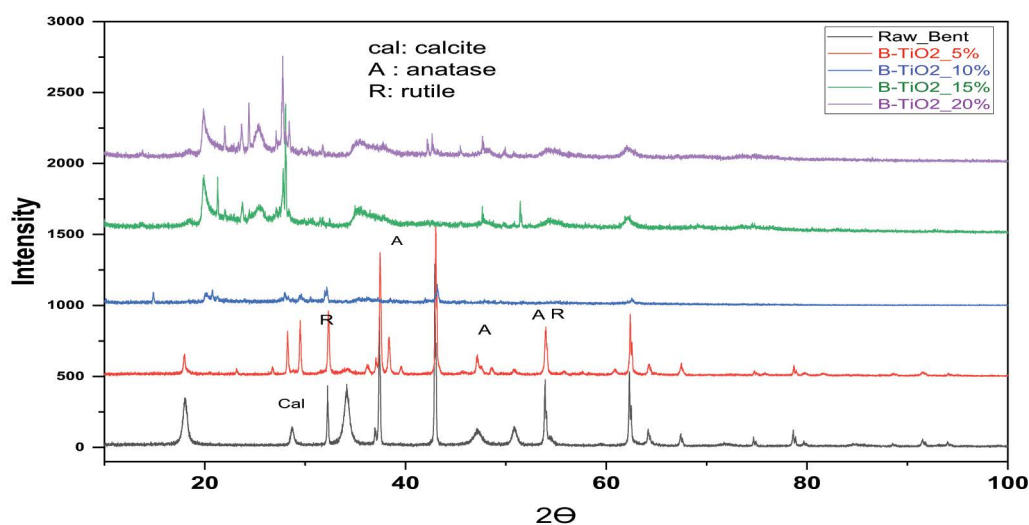


Fig. 1. X-ray diffraction patterns of Raw-B and TiO₂-B.

and $1,120\text{ cm}^{-1}$ corresponds to the stretching vibrations of Si–O–Si band. The frequencies 920 and $3,633.2\text{ cm}^{-1}$ were attributed to the stretching vibrations of the OH group and the stretching of Al_2OH (interaction between OH and Al). It was recorded that the bands between 600 and 700 cm^{-1} correspond to the presence of nanoparticles [9]. The bands correspond to Si–O, Si–O–M, and M–O–H (M = Al, Fe and Mg) liaisons were existed between anions and cations at octahedral or tetrahedral sites, as well as many OH groups. The middle band which extends between $3,600$ – $3,849\text{ cm}^{-1}$, with intense peaks at $3,640.6\text{ cm}^{-1}$, was characteristic of montmorillonite [35]. Between $3,620$ – $3,640\text{ cm}^{-1}$, the peak corresponds to the stretching vibrations of the bond of the O–H groups [35,36]. Comparing the spectra of Raw-B and TiO_2 -B, it was noted that there is a significant agreement except for the intensity of the peaks which have become more intense, as well as a small modification in the vibrational shifts of the TiO_2 -B. The bands 470.8 and 531.9 cm^{-1} due to the existence of Titanium, given the displacement of titanium oxide. The vibrations in the range 800 – 400 cm^{-1} group together the stretching vibrations of Si–O and Si–O–M band of the Raw-B. It was also observed that more the titanium oxide content increases, the vibrational band $3,600$ – $3,849\text{ cm}^{-1}$ becomes less intense, while, the vibration bands of valence 400 – 560 cm^{-1} and $1,048\text{ cm}^{-1}$ become intense [13].

To study the morphology and the chemical composition of Raw-B and TiO_2 -B, transmission electron microscopy/EDX was investigated and presented in Fig. 2. From Fig. 3a, c, e a hexagonal form and a plated structure is observed. The Moiré phenomenon was also detected showing the perfect crystallization of bentonite. While Fig. 3b shows the presence of oxygen, manganese, calcium and copper with traces of aluminum and carbon. The EDX analysis of TiO_2 -B 20% indicates that it was mainly composed of titanium, oxygen, copper and carbon associated with other minerals such as manganese, calcium, and sodium (Fig. 3d and f).

The specific surface was used to determine the real surface of samples, it was based on the phenomenon of gas or vapor adsorption at a given temperature for a certain pressure range. The specific surface area of Raw-B and TiO_2 -B was determined using diverse methods including BET (Brunauer–Emmett–Teller), BJH (Barrett–Joyner–Halenda), t -plot, and Langmuir. Table 2 collects the specific surface values of Raw-B and TiO_2 -B by different methods. The Langmuir model indicates that the TiO_2 content increases with the increase of the specific surface. Therefore, the specific surface obtained by BJH analysis was higher than the specific surface attained using BET.

The measurement of Raw-B and TiO_2 -B porosities are collected in Table 3. The porosities of Raw-B and TiO_2 -B were determined from the adsorption–desorption isotherms of N_2 according to the methods of BJH and t -plot [37]. According to Table 3, it was noted that the pore distribution was less than 50 nm , indicating the predominant presence of mesopores and that the increase of TiO_2 content when the predominant zone of the micropores was closer.

The laser granulometry allowed to analyze the size distribution of Raw-B and TiO_2 -B particles, it was found that the size distribution was around 0.1 and $1,000\text{ }\mu\text{m}$. According to Table 4, the coefficient of uniformity (CU) represents the ratio of larger grains diameter to that of lesser grains

assumed [38]. The coefficient of uniformity registers that the values were higher than 1, where the particles have a non-uniform distribution. It was observed that the doping rate decreases when the uniformity coefficient was approaching 1 and vice versa when the doping rate increases.

The quantities D_x (D_{10} , D_{50} and D_{90}) define the populations of the different diameters. The D_{10} was reduced from $93.159\text{ }\mu\text{m}$ for Raw-B to $9.827\text{ }\mu\text{m}$ for TiO_2 -B 20%, this decrease in diameter can be explained by the increase of fine particles volume and the supersaturation by the nanoscale particles of TiO_2 during doping processes. However, the calcination has no effect on the agglomeration of particles. Whereas, the stability of the average size D_{50} and the coarse size D_{90} , which probably due to the sequestration of TiO_2 particles in the micropores and the mesopores or between bentonite leaves.

3.2. Adsorption of MB and MO

3.2.1. Effect of TiO_2 ratio

The evolution of MB as a function of time shows that Raw-B or TiO_2 -B gives similar results in terms of final discoloration, which vary between 90% and 100%. Nevertheless, the initial speeds of adsorption are higher for Raw-B or TiO_2 -B doped at 5%, whereas they are lower for samples doped at higher rates. This can be explained by the occupation of the adsorption sites by the added TiO_2 .

Fig. 5 indicates that the reduction of MO on crude bentonite and B- TiO_2 does not exceed 18%. it can therefore be concluded that the doping alone of bentonite with titanium oxide has no effect on the reduction of MO.

3.2.2. Effect of contact time

We note that for this paragraph we have chosen to compare the adsorption of the two dyes on raw bentonite and bentonite doped with 20% titanium oxide. Fig. 6 shows the evolution of the reduction of dyes as a function of time. It concludes that the reduction rate of methyl orange does not exceed 18% under the reaction conditions, whereas it was 100% for methylene blue after 50 min of contact time.

Bentonite particles carry a negative structural charge [39], clearly alkaline ($8.5 < \text{pH} < 10$) [40], which increases the attraction action with methylene blue (cationic dye) and increases the repelling action with methyl orange. Methyl orange is an anionic dye with a sulfonic group which is responsible for the high solubility in water [41]. Therefore, the mechanism of adsorption is due to Van Der Waals and ionic forces.

The variation of the amount adsorbed in MO by the Raw-B and TiO_2 -B have the same value. The doping has practically no effect on the amount adsorbed. There is also a fluctuation in the quantity adsorbed in MO, which can be explained by an alternation of the adsorption/desorption.

3.2.3. Effect of hydrochloric acid (activation)

In the previous paragraph that the reduction rate of methyl orange did not exceed 18% whether on raw bentonite or doped with titanium oxide, for this an acid activation was tested, by adding 1 mL/L up to 4 mL/L of 38% HCl.

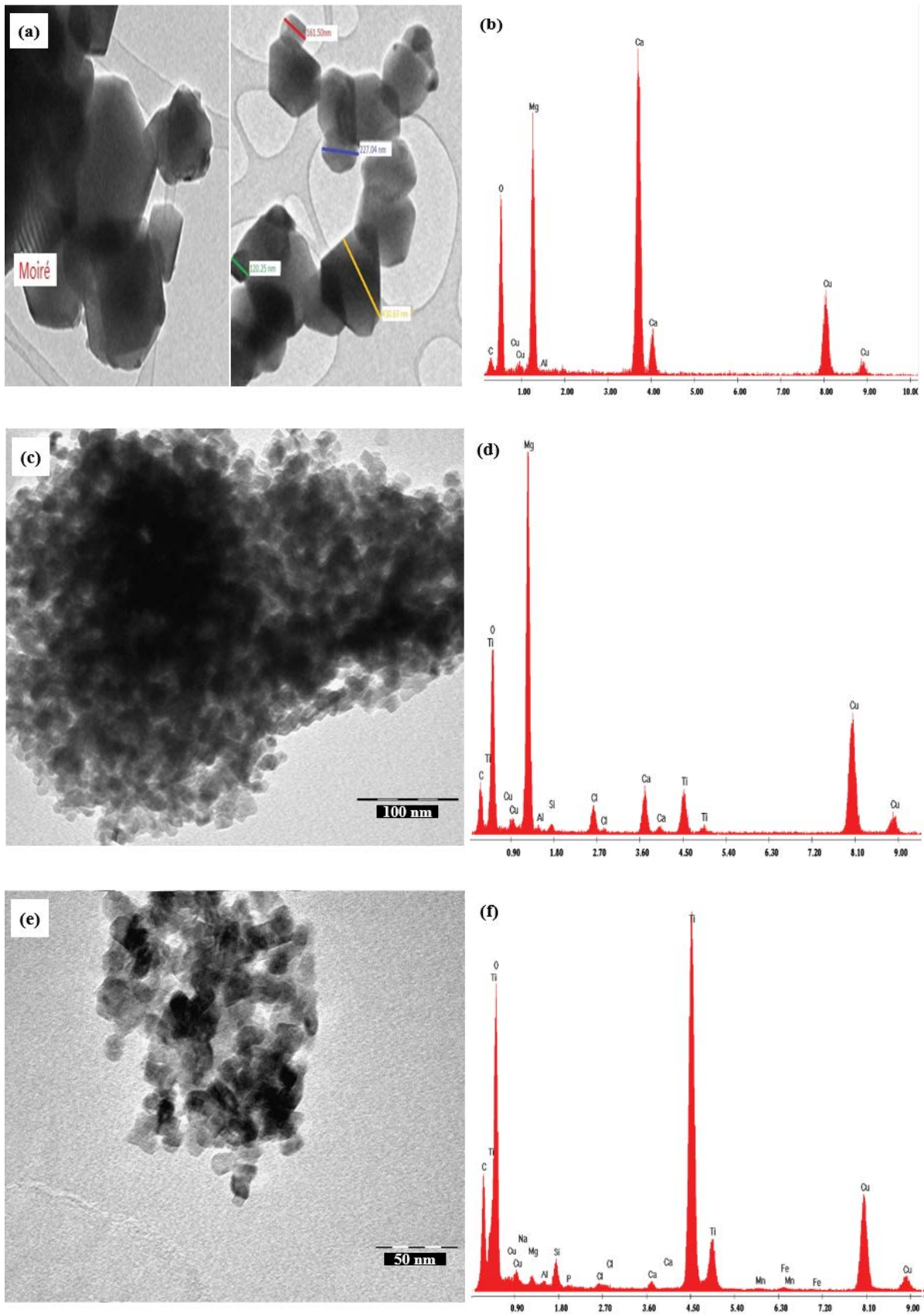


Fig. 3. Transmission electron microscopy/energy-dispersive X-ray spectroscopy of (a,b) Raw-B, (c,d) TiO₂-B at 15%, (e,f) TiO₂-B at 20%.

Table 2
Specific surfaces of TiO₂-B according to the doping rate

Matrix	BET (m ² /g)	Langmuir (m ² /g)	<i>t</i> -plot (m ² /g) adsorption	<i>t</i> -plot (m ² /g) desorption	BJH (m ² /g) adsorption	BJH (m ² /g) desorption
B-TiO ₂ (0%)	5.2759	7.1885	2.2236	3.0524	3.046	5.2610
B-TiO ₂ (5%)	7.0995	9.8838	0.8802	6.2192	6.451	7.6149
B-TiO ₂ (10%)	14.1722	19.2943	4.5090	9.6632	14.810	35.7084
B-TiO ₂ (15%)	57.5087	78.6217	12.4309	45.0777	52.525	75.5406
B-TiO ₂ (20%)	60.5175	82.9229	13.9548	46.5627	54.985	79.8989

Table 3
TiO₂-B pore diameters as a function of doping rate

Pore distribution	<i>t</i> -plot in nm	BJH adsorption in nm	BJH desorption in nm
B-TiO ₂ (0%)	12.071	40.250	23.972
B-TiO ₂ (5%)	14.846	39.360	33.239
B-TiO ₂ (10%)	15.881	25.745	10.600
B-TiO ₂ (15%)	8.788	11.672	8.234
B-TiO ₂ (20%)	9.862	13.853	9.655

Table 4
Average sizes of Raw-B and TiO₂-B at different levels of TiO₂

	TiO ₂ -B (0%)	TiO ₂ -B (5%)	TiO ₂ -B (10%)	TiO ₂ -B (15%)	TiO ₂ -B (20%)
D ₁₀ (μm)	93.159	67.246	19.176	13.381	9.827
D ₅₀ /D ₁₀	1.86	2.23	8.03	10.87	14.74
D ₅₀ (μm)	173.573	150.150	153.985	150.024	144.892
D ₉₀ (μm)	305.947	255.506	300.754	303.817	300.842
D ₉₀ /D ₅₀	1.76	1.70	1.95	2.03	2.08

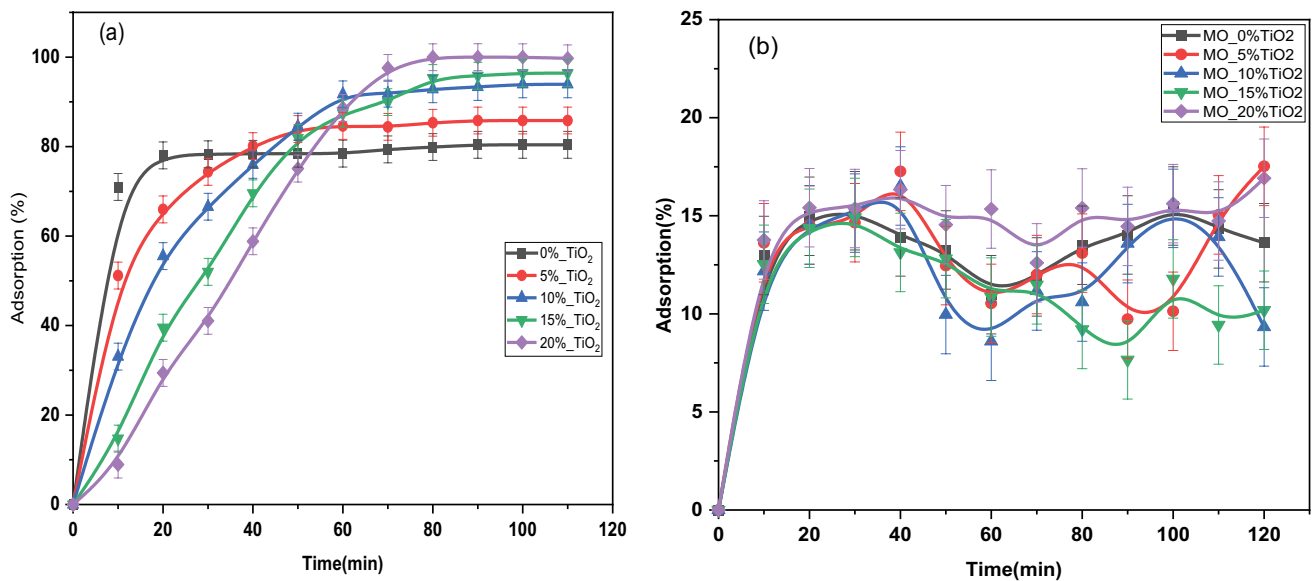


Fig. 4. Effect of TiO₂ ratio on the adsorption of (a) MB and (b) MO ($V = 500$ mL, $m = 1$ g/L, $C_{MB} = 120$ mg/L, $C_{MO} = 40$ mg/L, $T = 25^\circ\text{C}$).

The best MO adsorption results were recorded (95%) for an addition of 4 mL/L of hydrochloric acid. Indeed, activation is a complex process that involves a series of chemical reactions, and the result is an increase in the specific surface. The latter goes from 40–60 to almost 200 m² for dry clay [42]. The variation in the quantity adsorbed in MO by the activated TiO₂-B and Raw-B activated by adding HCl, is illustrated in the following for a concentration of 140 mg/L of methyl orange.

It can be seen that the acid activation of TiO₂-B at different doping percentage (0%, 5%, 10%, 15% and 20%) allows an increase significant amount of this dye

adsorbed, which makes it possible to obtain an abatement rate of nearly 98%.

3.2.4. Adsorption kinetics

The kinetics of the decolorization reaction were undertaken, on one hand with MB on TiO₂-B doped at 5% and on the other hand with MO in a medium activated by HCl. For this, 1 g of TiO₂-B was placed in 1 L of aqueous solution having a dye concentration of 40 mg/L. The obtained results are shown in Fig. 7. It's noted that the reaction rate is fast at the beginning of the process and becomes increasingly

slow until reaching equilibrium. The reaction equilibrium times for the dyes studied are 30 min for methylene blue whereas for MO, the process is unstable, the evolution of the quantity as a function of time shows oscillations probably due to the phenomenon of adsorption.

To get closer to the reaction mechanism and determine the different kinetic parameters, we used the Lagergren equations, based on (Fig. 7a and b), the first and second-order kinetic. Fig. 7 shows the linear forms of the first and second-order kinetic models, respectively.

The kinetic parameters (Table 5) indicate that the values of the correlation coefficient (R^2) for the first-order model is closer to 1 than that of the second-order model. Thus, the best description of the adsorption kinetics is obtained by the pseudo-first-order model, in the literature, this type of isotherm is characteristic of adsorption on microporous carbons and zeolites [12].

3.2.5. Adsorption isotherms

The adsorption isotherms were carried out with different initial concentrations of dye with 1 g/l of TiO_2 -B

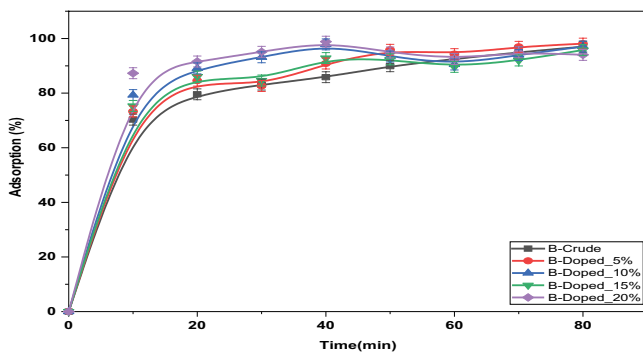


Fig. 5. Reduction of MO ($C_{\text{methylene orange}} = 140 \text{ mg/L}$) by doped and activated bentonite.

doped with 5% TiO_2 for methylene blue and by adding HCl to the medium for methyl orange. The contact time is 15 min at 25°C.

Fig. 8 represents the adsorption isotherms of the two dyes. These isotherms are compared to the models present in the literature, then the constants characterizing each of the systems are then determined in Table 6.

The MB adsorption isotherm indicates that the adsorption is very important and type L in the classification of

Table 5
Adsorption rate constants for the two models

Bentonite	Dye	Pseudo-first-order model		Pseudo-second-order model	
		k_1	r_1^2	k_2	r_2^2
Doped	MB	0.081	0.881	0.098	0.885
Doped and activated	MO	0.065	0.841	0.029	0.787

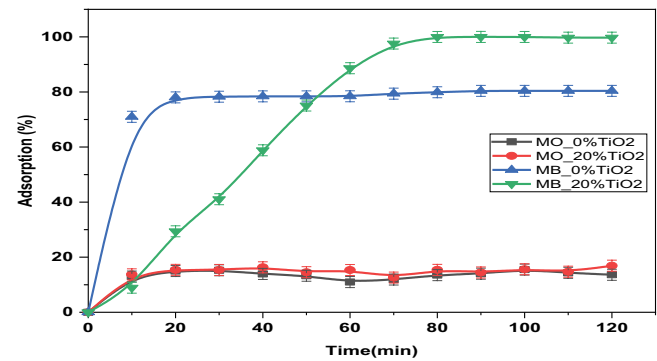


Fig. 6. Effect of contact time on the adsorption of MB and MO onto Raw-B and TiO_2 -B 20% ($V = 500 \text{ mL}$, $m = 1 \text{ g/L}$, $C_{\text{MB}} = 120 \text{ mg/L}$, $C_{\text{MO}} = 40 \text{ mg/L}$, $T = 25^\circ\text{C}$).

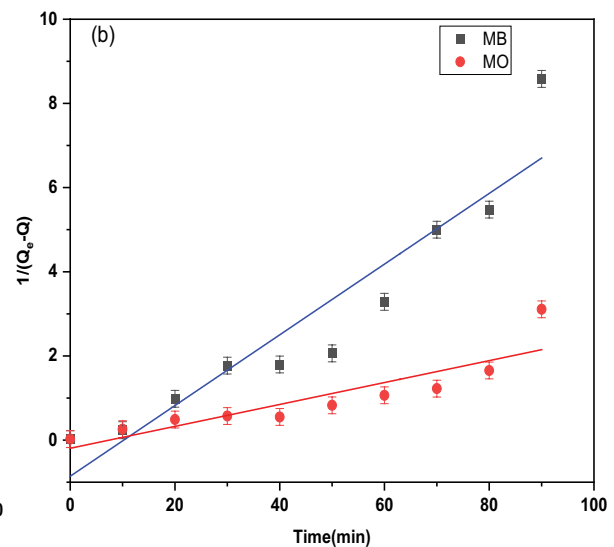
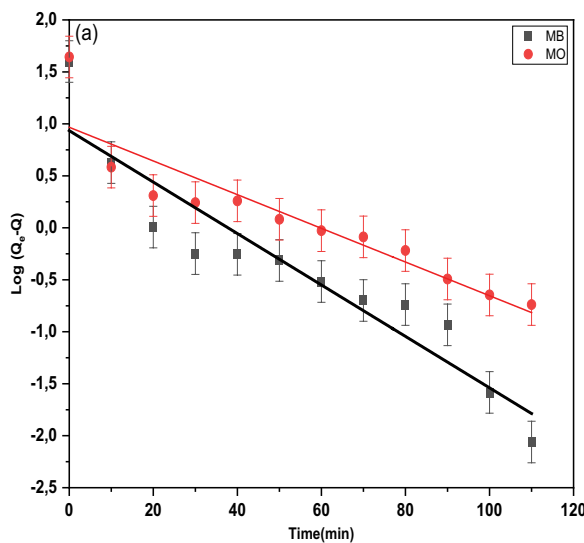


Fig. 7. Kinetic study of MB and MO adsorption (a) pseudo-first-order and (b) pseudo-second-order.

Giles et al. [43,44]. This type of isotherm is usually associated with ionic adsorption in solution with weak competition with solvent molecules [43]. The best correlation for this dye is obtained with the Langmuir model ($R^2 = 0.999$) and the Freundlich model ($R^2 = 0.944$). The maximum adsorption capacity is 60.976 mg/g. These results indicate that MB is probably homogeneously adsorbed using ionic interactions mediated by the doped, negatively charged bentonite surface [45].

The initial part of the MO adsorption isotherm is almost vertical, the adsorbed quantity appears significant at almost zero solute concentration in the solution. This phenomenon occurs when the interactions between the adsorbed molecules and the surface of the solid are very strong. This is a class II isotherm. In the bibliography, the type II isotherm can also result from a sum of isotherms I+II. (Filling of micropores followed by a multilayer adsorption on an external surface [18]. The best correlation for this dye is obtained with the two models. The maximum adsorption capacity is 142.857 mg/g. The values of the constants K , Q_{max} , K_F and $1/n$ are grouped in Table 6.

3.3. Photocatalytic degradation of MB and MO

The TiO₂-B (20%) samples were tested in terms of photocatalytic activities in the absence and presence of UV light, using two lamps of wavelength 245 and 365 nm, it is noticed that the evolution of the MB color reduction rate as a function of the irradiation time of the 245 nm lamp is maximum (100%) after 70 min. With the 365 nm lamp or without UV irradiation, the reduction rate is about 90% but with an equilibrium time of 80 min. Comparing these results

Table 6
Constants of adsorption isotherm models for the two dyes

Isotherm model	Langmuir model			Freundlich model		
	Q_m (mg/g)	K_L (L/g)	R^2	$1/n_F$	K_F (L/g)	R^2
MB	60.976	8.197	0.999	0.174	5.26	0.944
MO	142.857	0.365	0.759	0.594	4.45	0.943

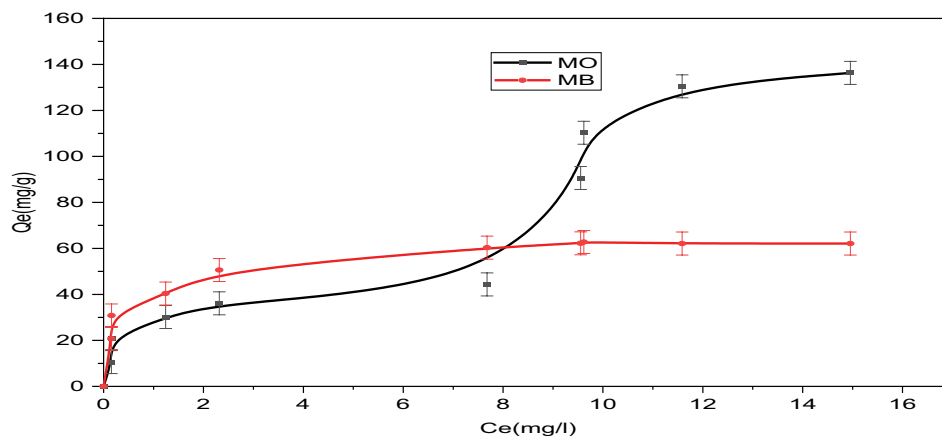


Fig. 8. Amount of MB and MO adsorbed according to the initial concentration.

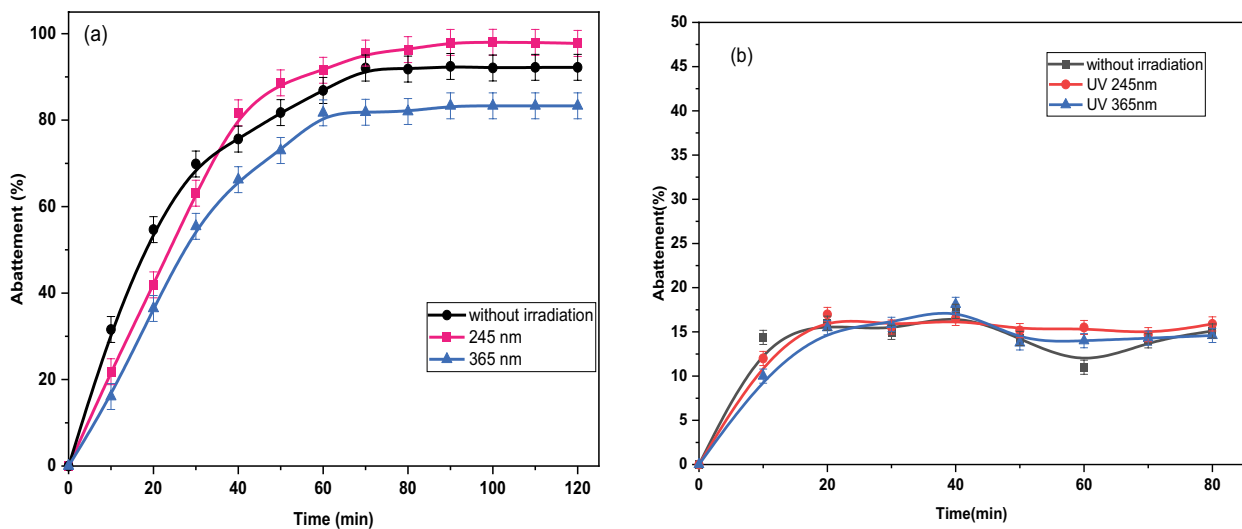


Fig. 9. Effect of source irradiation on the photodegradation of MB (a) and MO (b).

(Fig. 9a) with the adsorption results obtained in Fig. 6, it can be concluded that the abatement rate of the photo catalytic degradation is 20% for methylene blue.

For the activated MO Fig. 9b, we notice that there is no difference between the degradation in the absence or in the presence of UV light flux irradiation (245 nm, 365 nm) with TiO₂-B.

4. Conclusion

The chemical analysis of TiO₂-B shows that the titanium oxide doping is not stoichiometric, but it obeys a linear law with a correlation coefficient $R = 0.98$. The physico-chemical characterization reveals two well crystallized allotropic forms: anatase and rutile. The adsorption isotherms indicate a progressive increase in the specific surface while increasing the content of titanium oxide in TiO₂-B. The treatment of methylene blue with TiO₂-B was carried out for different levels of doping with titanium oxide and reached 100% for a doping of 15% with TiO₂. Methyl orange recorded a reduction of less than 20%, but after adding HCl, a rate of 100% was reached with a low release. The study shows that the adsorption isotherms of methylene blue on doped or undoped bentonite are modeled satisfactorily for the Langmuir and Freundlich models, while for methyl orange it only obeys to the model of Langmuir.

References

- [1] O. Lefebvre, R. Moletta, Treatment of organic pollution in industrial saline wastewater: a literature review, *Water Res.*, 40 (2006) 3671–3682.
- [2] C. Baird, Toxic organic chemicals, *Environ. Chem.*, (1995) 215–230.
- [3] S. Mehra, M. Singh, P. Chadha, Adverse impact of textile dyes on the aquatic environment as well as on human beings, *Toxicol. Int.*, 28 (2021) 165–176.
- [4] D.C. Kalyani, A.A. Telke, S.P. Govindwar, J.P. Jadhav, Biodegradation and detoxification of reactive textile dye by isolated *Pseudomonas* sp. SUK1, *Water Environ. Res.*, 81 (2009) 298–307.
- [5] S.H. Hashemi, M. Kaykhaii, Azo Dyes: Sources, Occurrence, Toxicity, Sampling, Analysis, and Their Removal Methods, T. Dalu, N.T. Tavengwa, Eds., *Emerging Freshwater Pollutants: Analysis, Fate and Regulations*, Elsevier, 2022, pp. 267–287.
- [6] B.L. Alderete, J. da Silva, R. Godoi, F.R. da Silva, S.R. Taffarel, L.P. da Silva, A.L.H. Garcia, H. Mitteregger Júnior, H.L. Neubauer de Amorim, J.N. Picada, Evaluation of toxicity and mutagenicity of a synthetic effluent containing azo dye after advanced oxidation process treatment, *Chemosphere*, 263 (2021) 128291, doi: 10.1016/j.chemosphere.2020.128291.
- [7] N.F. Cardoso, E.C. Lima, B. Royer, M.V. Bach, G.L. Dotto, L.A.A. Pinto, T. Calvete, Comparison of *Spirulina platensis* microalgae and commercial activated carbon as adsorbents for the removal of Reactive Red 120 dye from aqueous effluents, *J. Hazard. Mater.*, 241–242 (2012) 146–153.
- [8] S. Belaidi, M. Mellaoui, Electronic structure and physical-chemistry property relationship for oxazole derivatives by Ab initio and DFT methods, *Org. Chem. Int.*, 2011 (2011) 254064, doi: 10.1155/2011/254064.
- [9] N.A. Mohammed, A.I. Alwared, M.S. Salman, Photocatalytic degradation of reactive yellow dye in wastewater using H₂O₂/TiO₂/UV technique, *Iraqi J. Chem. Pet. Eng.*, 21 (2020) 15–21.
- [10] Z. Al-Qodah, Adsorption of dyes using shale oil ash, *Water Res.*, 34 (2000) 4295–4303.
- [11] H. Chen, Y.J. Zhang, P.Y. He, C.J. Li, H. Li, Coupling of self-supporting geopolymer membrane with intercepted Cr(III) for dye wastewater treatment by hybrid photocatalysis and membrane separation, *Appl. Surf. Sci.*, 515 (2020) 146024, doi: 10.1016/j.apsusc.2020.146024.
- [12] B. Khan, B. Nawaz, M. Waseem, R. Hussain, S. Arif, G.J. Price, S. Haq, W. Rehman, Adsorption of methylene blue onto size controlled magnetite nanoparticles, *Mater. Res. Express*, 6 (2019) 095511, doi: 10.1088/2053-1591/ab2ef9.
- [13] B. Bayat, Comparative study of adsorption properties of Turkish fly ashes. I. The case of nickel(II), copper(II) and zinc(II), *J. Hazard. Mater.*, 95 (2002) 275–290.
- [14] A. Merakchi, S. Bettayeb, N. Drouiche, L. Adour, H. Lounici, Cross-linking and modification of sodium alginate biopolymer for dye removal in aqueous solution, *Polym. Bull.*, 76 (2019) 3535–3554.
- [15] A. Maleki, M. Mohammad, Z. Emdadi, N. Asim, M. Azizi, J. Safaei, Adsorbent materials based on a geopolymer paste for dye removal from aqueous solutions, *Arabian J. Chem.*, 13 (2020) 3017–3025.
- [16] M. Zubair, N.D. Mu'azu, N. Jarrah, N.I. Blaisi, H.A. Aziz, M.A. Al-Harathi, Adsorption behavior and mechanism of methylene blue, Crystal Violet, Eriochrome Black T, and methyl orange dyes onto biochar-derived date palm fronds waste produced at different pyrolysis conditions, *Water Air Soil Pollut.*, 231 (2020) 240, doi: 10.1007/s11270-020-04595-x.
- [17] M. El Alouani, S. Alehyen, H. El Hadki, H. Saufi, A. Elhalil, O.K. Kabbaj, M. Taibi, Synergetic influence between adsorption and photodegradation of Rhodamine B using synthesized fly ash based inorganic polymer, *Surf. Interfaces*, 24 (2021) 101136, doi: 10.1016/j.surfin.2021.101136.
- [18] K. Priyanka, N. Remya, M. Behera, Comparison of titanium dioxide based catalysts preparation methods in the mineralization and nutrients removal from greywater by solar photocatalysis, *J. Cleaner Prod.*, 235 (2019) 1–10.
- [19] K. Al-Hamoud, M.R. Shaik, M. Khan, H.Z. Alkhathlan, S.F. Adil, M. Kuniyil, M.E. Assal, A. Al-Warthan, M.R.H. Siddiqui, M.N. Tahir, S.T. Khan, A.A. Mousa, M. Khan, *Pulicaria undulata* extract-mediated eco-friendly preparation of TiO₂ nanoparticles for photocatalytic degradation of methylene blue and methyl orange, *ACS Omega*, 7 (2022) 4812–4820.
- [20] I. Block, C. Günter, A. Duarte Rodrigues, S. Paasch, P. Hessemann, A. Taubert, Carbon adsorbents from spent coffee for removal of methylene blue and methyl orange from water, *Materials*, 14 (2021) 3996, doi: 10.3390/ma14143996.
- [21] M.A. Ahmad, N.B. Ahmed, K.A. Adegoke, O.S. Bello, Sorption studies of methyl red dye removal using lemon grass (*Cymbopogon citratus*), *Chem. Data Collect.*, 22 (2019) 100249, doi: 10.1016/j.cdc.2019.100249.
- [22] X. Jin, B. Yu, Z. Chen, J.M. Arocena, R.W. Thring, Adsorption of Orange II dye in aqueous solution onto surfactant-coated zeolite: characterization, kinetic and thermodynamic studies, *J. Colloid Interface Sci.*, 435 (2014) 15–20.
- [23] M. Basibuyuk, C.F. Forster, An examination of the adsorption characteristics of a basic dye (Maxilon Red BL-N) on to live activated sludge system, *Process Biochem.*, 38 (2003) 1311–1316.
- [24] S. Dhiman, B. Gupta, Co₃O₄ nanoparticles synthesized from waste Li-ion batteries as photocatalyst for degradation of methyl blue dye, *Environ. Technol. Innovation*, 23 (2021) 101765, doi: 10.1016/j.eti.2021.101765.
- [25] D. Wattanasiriwech, K. Yomthong, S. Wattanasiriwech, Adsorption efficiency and photocatalytic activity of fly ash-based geopolymer foam mortar, *Ceram. Int.*, 47 (2021) 27361–27371.
- [26] E. Oyarce, B. Butter, P. Santander, J. Sánchez, Polyelectrolytes applied to remove methylene blue and methyl orange dyes from water via polymer-enhanced ultrafiltration, *J. Environ. Chem. Eng.*, 9 (2021) 106297, doi: 10.1016/j.jece.2021.106297.
- [27] R. Stanley, J. Alphas Jebasingh, S. Manisha Vidyavathy, P. Kingston Stanley, P. Ponmani, M.E. Shekinah, J. Vasanthi, Excellent photocatalytic degradation of methylene blue, Rhodamine B and methyl orange dyes by Ag-ZnO nanocomposite under natural sunlight irradiation, *Optik*, 231 (2021) 166518, doi: 10.1016/j.ijleo.2021.166518.
- [28] Y.J. Zhang, P.Y. He, H. Chen, L.C. Liu, Green transforming metallurgical residue into alkali-activated silicomanganese

- slag-based cementitious material as photocatalyst, *Materials*, 11 (2018) 1773, doi: 10.3390/ma11091773.
- [29] M.V. Diamanti, B. Del Curto, M. Ormellesse, M.P. Pedferri, Photocatalytic and self-cleaning activity of colored mortars containing TiO_2 , *Constr. Build. Mater.*, 46 (2013) 167–174.
- [30] V.Q. Hieu, T.K. Phung, T.-Q. Nguyen, A. Khan, V.D. Doan, V.A. Tran, V.T. Le, Photocatalytic degradation of methyl orange dye by $\text{Ti}_3\text{C}_2\text{-TiO}_2$ heterojunction under solar light, *Chemosphere*, 276 (2021) 130154, doi: 10.1016/j.chemosphere.2021.130154.
- [31] V.A. Tran, A.N. Kadam, S.-W. Lee, Adsorption-assisted photocatalytic degradation of methyl orange dye by zeolite-imidazole-framework-derived nanoparticles, *J. Alloys Compd.*, 835 (2020) 155414, doi: 10.1016/j.jallcom.2020.155414.
- [32] A. Oussalah, A. Boukeeroui, Study of methylene blue Adsorption in Aqueous Solution Using Alginate-Bentonite Beads, A. Kallel, M. Ksibi, H. Ben Dhia, N. Khélifi, Eds., *Recent Advances in Environmental Science from the Euro-Mediterranean and Surrounding Regions. EMCEI 2017, Advances in Science, Technology & Innovation*, Springer, Cham, 2018. Available at: https://doi.org/10.1007/978-3-319-70548-4_57
- [33] Q.H. Hu, S.Z. Qiao, F. Haghseresht, M.A. Wilson, G.Q. Lu, Adsorption study for removal of Basic Red dye using bentonite, *Ind. Eng. Chem. Res.*, 45 (2006) 733–738.
- [34] Ö. Muhammed, The effect of strontium carbonate additive on the production of graphitic boron nitride using modified O'connor method, *Cumhuriyet Sci. J.*, 42 (2021) 836–842.
- [35] L. Zeng, H. Sun, T. Peng, X. Lv, Comparison of the phase transition and degradation of methylene blue of TiO_2 , TiO_2 /montmorillonite mixture and TiO_2 /montmorillonite composite, *Front. Chem.*, 7 (2019) 538, doi: 10.3389/fchem.2019.00538.
- [36] R. Bassam, M. El Alouani, J. Maissara, N. Jarmouni, M. Belhabra, M. El Mahi Chbihi, S. Belaouad, Investigation of competitive adsorption and desorption of heavy metals from aqueous solution using raw rock: characterization kinetic, isotherm, and thermodynamic, *Mater. Today Proc.*, 52 (2022) 158–165.
- [37] J. Pires, R. Fernandes, M.L. Pinto, M. Batista, Microporous volumes from nitrogen adsorption at 77 K: when to use a different standard isotherm?, *Catalysts*, 11 (2021) 1544, doi: 10.3390/catal11121544.
- [38] C. Shen, S. Liu, L. Wang, Y. Wang, Micromechanical modeling of particle breakage of granular materials in the framework of thermomechanics, *Acta Geotech.*, 14 (2019) 939–954.
- [39] K.E. Yoboue, K.P. Kouadio, A.D.L. Kabore, A. Yao-Kouame, Nature minéralogique et niveau d'évolution d'un Cambisol développé sur schiste dans la région d'Azaguié, Sud-Est de la Côte d'Ivoire, *Int. J. Innovation Appl. Stud.*, 26 (2019) 1170–1179.
- [40] F.E. Otitigbe, Evaluation of pH of drilling fluid produced from local clay and additives, *J. Appl. Sci. Environ. Manage.*, 25 (2021) 561–566.
- [41] R.K. Ibrahim, A. El-Shafie, L.S. Hin, N.S.B. Mohd, M.M. Aljumaily, S. Ibraim, M.A. AlSaadi, A clean approach for functionalized carbon nanotubes by deep eutectic solvents and their performance in the adsorption of methyl orange from aqueous solution, *J. Environ. Manage.*, 235 (2019) 521–534.
- [42] L. Laysandra, I.J. Ondang, Y.-H. Ju, B.H. Ariandini, A. Mariska, F.E. Soetaredjo, J.N. Putro, S.P. Santoso, F.L. Darsono, S. Ismadji, Highly adsorptive chitosan/saponin-bentonite composite film for removal of methyl orange and Cr(VI), *Environ. Sci. Pollut. Res.*, 26 (2019) 5020–5037.
- [43] K. Boughzala, F. Kooli, N. Meksi, A. Bechrifa, K. Bouzouita, Waste products from the phosphate industry as efficient removal of Acid Red 88 dye from aqueous solution: their regeneration uses and batch design adsorber, *Desal. Water Treat.*, 202 (2020) 410–419.
- [44] F. Wang, Y. Gao, Y. Liu, X. Zhang, X. Gu, D. Ma, Z. Zhao, Z. Yuan, H. Xue, H. Liu, BES1-regulated BEE1 controls photoperiodic flowering downstream of blue light signaling pathway in *Arabidopsis*, *New Phytol.*, 223 (2019) 1407–1419.
- [45] S. Amri, R. Hayder, K. Diaf, M. Kamoun, et N. Besbes, Contribution de catalyseurs inorganiques et d'argiles en synthèse de composés organiques, *RHAZES: Green Appl. Chem.*, 15 (2022) 3–16.